



A 3D, Multiphase, Multicomponent Model of the Cathode and Anode of a PEM Fuel Cell

T. Berning and N. Djilali^z

Institute for Integrated Energy Systems, University of Victoria, Victoria, British Columbia V8W 3P6, Canada

A computational fluid dynamics multiphase model of a proton-exchange membrane (PEM) fuel cell is presented. The model accounts for three-dimensional transport processes including phase change and heat transfer, and includes the gas-diffusion layers (GDL) and gas flow channels for both anode and cathode, as well as a cooling channel. Transport of liquid water inside the gas-diffusion layers is modeled using viscous forces and capillary pressure terms. The physics of phase change is accounted for by prescribing local evaporation as a function of the undersaturation and liquid water concentration. Simulations have been performed for fully humidified gases entering the cell. The results show that different competing mechanisms lead to phase change at both anode and cathode sides of the fuel cell. The predicted amount of liquid water depends strongly on the prescribed material properties, particularly the hydraulic permeability of the GDL. Analysis of the simulations at a current density of 1.2 A/cm² show that both condensation and evaporation take place within the cathode GDL, whereas condensation prevails throughout the anode, except near the inlet. The three-dimensional distribution of the reactants and products is evident, particularly under the land areas. For the conditions investigated in this paper, the liquid water saturation does not exceed 10% at either anode or cathode side, and increases nonlinearly with current density.

© 2003 The Electrochemical Society. [DOI: 10.1149/1.1621412] All rights reserved.

Manuscript submitted January 13, 2003; revised manuscript received June 9, 2003. Available electronically November 12, 2003.

The operation of proton-exchange membrane (PEM) fuel cells depends not only on the effective distribution of air and hydrogen, but also on the maintenance of an adequate cell operating temperature and fully humidified conditions in the membrane. The fully humidified state of the membrane is crucial to ensuring good ionic conductivity and is achieved by judicious water management. Water content is determined by the balance between various water transport mechanisms and water production. The water transport mechanisms are electro-osmotic drag of water (*i.e.*, motion of water molecules attaching to protons migrating through the membrane from anode to cathode); back diffusion from the cathode (due to nonuniform concentration); and diffusion and convection to/from the air and hydrogen gas streams. Water production depends on the electric current density and phase change. Without control, an imbalance between production and removal rates of water can occur. This can result in either dehydration of the membrane, or flooding of the electrodes, which are both detrimental to performance.

A common water management technique relies on the humidification of the air and hydrogen gas streams. At higher current densities, the excess product water is removed by convection via the air stream, and the rate of removal is controlled by adjusting moisture content in concert with pressure drop and temperature in the flow channels. Thermal management is also required to remove the heat produced by the electrochemical reaction in order to prevent drying out of the membrane, which in turn can result not only in reduced performance but also in eventual rupture of the membrane. Thermal management, which is performed via forced convection cooling in larger stacks, is also essential for the control of the water evaporation or condensation rates.

The operation of a fuel cell and the resulting water and heat distributions depend on numerous transport phenomena including charge-transport and multicomponent, multiphase flow, and heat transfer in porous media. The complexity and interaction of these processes and the difficulty in making detailed *in situ* measurements have prompted the development of a number of numerical models. The theoretical framework was laid out in early one-dimensional numerical models of the membrane-electrode.¹⁻³ A quasi-two-dimensional model based on concentrated solution theory was also proposed by Newman and Fuller,⁴ and a full two-dimensional model including flow channels but no electrodes was also presented by Nguyen and White.⁵ This model was refined in a number of subsequent studies to account for the porous electrodes and interdigitated gas distribution.^{6,7}

One of the first models accounting fully for transport in the gas distribution channels and applying the methods of computational fluid dynamics for PEM fuel cell was published by Gurau *et al.*⁸ This 2D steady-state model included both the MEA and the gas flow channels and considered the gas-liquid phases in separate computational domains, *i.e.*, the interaction between both phases was not considered. A similar model was also presented by Um *et al.*⁹ With the exception of Ref. 10, the three-dimensional models reported in the literature were mostly developed using commercial computational fluid dynamic (CFD) codes.¹¹⁻¹⁴ These models provide comprehensive details on the distribution of reactants and allow sensitivity analysis and prediction of performance under various conditions, but they do not account for phase change and liquid water concentration in the electrodes.

Models providing information on liquid-water saturation/flooding include the one-dimensional steady-state model of Baschuk and Li¹⁵ in which the degree of water flooding was determined by matching the predictions to the experimental polarization curve using a trial-and-error method. Shimpalee *et al.*¹⁶ extended their single-phase 3D model to account for liquid water as a component of the fluid mixture. The impact of liquid water on transport in the gas-diffusion electrode was, however, not accounted for. Nguyen's group presented a 2D multiphase transport model of the cathode gas-diffusion layer.¹⁷ The other important contributions are the 2D multiphase cathode models^{18,19} based on Wang's two-phase flow mixture theory.²⁰ In this approach, each species/phase in the porous electrode is modeled using an individual mass conservation equation, but a single momentum equation is solved to obtain the velocity field of the entire mixture. This means that each component is convected according to the global mixture velocity and diffused according to a unique diffusivity tensor. The liquid water and vapor concentrations are determined *a posteriori* based on the temperature and pressure field. In addition to being restricted to 2D and the cathode side of a cell, the simulations presented so far using the mixture model are restricted to low humidity inlet feed streams.

Overall, the coupling of computational fluid dynamics methodologies with electrochemistry has allowed the development of increasingly more representative fuel cell models. In the present work several new steps have been taken: (i) the model accounts fully for three-dimensional transport and two-phase flow; (ii) both cathode and anode are included; (iii) the two-phase model accounts for momentum transport in the liquid and gas phase through separate transport equations and includes exchange terms between phases. This model was implemented into the commercial code CFX 4.3, and numerical simulations corresponding to operation with high hu-

^z E-mail: ndjilali@uvic.ca

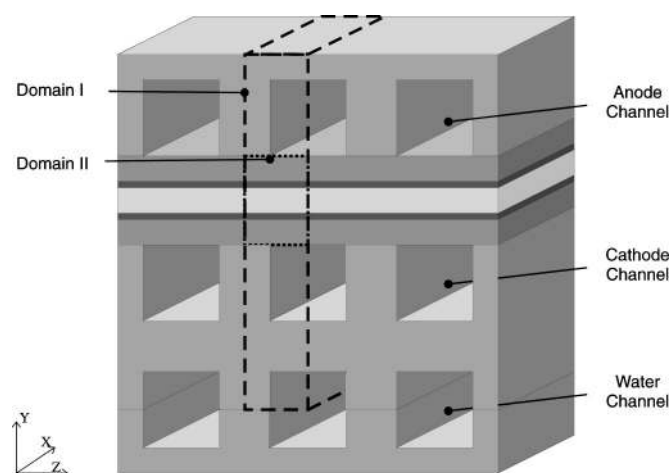


Figure 1. Computational domain employed for the multiphase model. The membrane is currently considered a heat-conducting solid.

midity inlet are presented and analyzed. The simulations provide insight into the phase-change mechanisms at the cathode sides and reveal some interesting multiphase effects at the anode.

Model Description

Model assumptions.—A schematic of the domain modeled is shown in Fig. 1. The model includes both anode and cathode, the reactant flow channels as well as a water cooling channel. Transport and gradients in all three-directions are accounted for. The framework of the single-phase PEM fuel cell model described in Ref. 14 was used. In this paper we focus on modeling of two-phase transport and phase change in the electrodes and the prediction of the onset of pore plugging or flooding under various operating conditions.

The following assumptions are made in implementing the two-phase model: (i) no liquid water enters the cells at the inlets; (ii) the gases entering the cell are fully humidified; (iii) the product water is in the liquid phase; (iv) two-phase flow inside the porous media can be described by the unsaturated flow theory (UFT);²⁰ (v) the liquid phase and the gas phase share the same pressure field inside the flow channels; and (vi) both phases occupy a certain local volume fraction inside the porous media and their interaction is accounted for through a multifluid approach.

In addition to three-dimensionality and the inclusion of both anode and cathode, the present model differs substantially from earlier studies in that momentum transport in the liquid and gas phase is accounted for through separate transport equations that include exchange terms between phases. It should be noted that the anodes and cathode transport are decoupled. The coupling of the two sides would significantly add to the computational cost and complexity of an already very involved problem and would also require a detailed membrane model accounting fully for the variation of transport properties as a function of water content and temperature.

Modeling domain.—Symmetry conditions are applied at the boundaries in the y direction and the z direction; thus only half of a gas-flow channel needs to be modeled and a quarter of the water cooling channel. This reduces computational requirements for this complex problem. Two separate computational domains have to be set up for the gas-diffusion layers. Domain I consists of the gas-flow channels, separated by the impermeable membrane and the graphite plates, and domain II consists of the gas-diffusion layers to accommodate the heat transfer through the solid matrix of the porous medium.

Modeling equations.—The model is implemented in a commercial Computational Fluid Dynamics codes *CFX 4* using a set of custom written user subroutines. The code uses the finite volume

approach to solve the discretized Navier-Stokes equations and generic transport equation. The mathematical model for the gas phase is essentially identical to the single-phase model presented in an earlier study¹⁴ with the addition of exchange terms associated with phase change and modified permeability as discussed below. We therefore focus on describing the modeling and implementation of the liquid water transport and phase change.

Gas flow channels.—The liquid water flow inside the gas-flow channels is governed by the Navier-Stokes equations for an incompressible fluid. The continuity equation for the liquid water inside the channel is given by

$$\nabla \cdot (\mathbf{r}_l \rho_l \mathbf{u}_l) = 0 \quad [1]$$

where \mathbf{r}_l denotes the volume fraction of the liquid water, ρ_l is the density, and \mathbf{u}_l is the velocity vector. The momentum equation is the standard momentum equation for an incompressible Newtonian fluid

$$\nabla \cdot \{[\rho \mathbf{u}_l \times \mathbf{u}_l - \mu(\nabla \mathbf{u}_l + (\nabla \mathbf{u}_l)^T)]\} = -r_l \nabla p \quad [2]$$

Gas-diffusion layers.—In practice it is expected that most of the phase change will take place in the porous gas diffusion electrodes. The physics of multiple phases through a porous medium, which is challenging in itself, is further complicated here with phase change and the sources and sinks associated with the electrochemical reaction. The equations used to describe transport in the gas-diffusion layers are given below.

Mass transfer in the form of evaporation ($\dot{m}_{\text{phase}} > 0$) and condensation ($\dot{m}_{\text{phase}} < 0$) is assumed, so that the mass balance equations for both phases read

$$\nabla \cdot [(1 - s)\epsilon \rho_g \mathbf{u}_g] = \dot{m}_{\text{phase}} \quad [3]$$

and

$$\nabla \cdot (s \epsilon \rho_l \mathbf{u}_l) = \dot{m}_{\text{phase}} \quad [4]$$

Note that the saturation s is identical to the liquid water volume fraction r_l and is introduced here simply to keep with the accepted nomenclature. Since the sum of all volume fractions has to equal unity, the volume fraction of the gas-phase r_g is equivalent to $(1 - s)$.

The momentum equation for the gas phase reduces to Darcy's law, which in this case is based on the relative permeability for the gas phase k_p^g . The relative permeability accounts for the reduction in pore space available for one phase due to the existence of the second phase. Different approaches can be used to mathematically describe the relative permeability, the simplest of which is²¹

$$k_p^g = (1 - s)k_p^0 \quad [5]$$

and

$$k_p^l = s k_p^0 \quad [6]$$

where k_p^0 is the permeability of the dry electrode and s is again the saturation of liquid water inside the GDL. With this, the momentum equation for the gas phase reduces to

$$\mathbf{u}_g = -\frac{k_p^g}{\mu_g} \nabla p_g = -(1 - s) \frac{k_p^0}{\mu_g} \nabla p_g \quad [7]$$

Two liquid water transport mechanisms are considered; shear, which drags the liquid phase along with the gas phase in the direction of the pressure gradient, and capillary forces, which drive liquid water from high to low saturation regions.²¹ Starting from Darcy's law we can write

$$\mathbf{u}_l = -\frac{k_p^l}{\mu_l} \nabla p_l \quad [8]$$

where the liquid water pressure stems from the gas-phase pressure and the capillary pressure according to²⁰

$$\nabla p_l = \nabla p_g - \nabla p_c = \nabla p_g - \frac{\partial p_c}{\partial s} \nabla s \quad [9]$$

Introducing this expression into Eq. 8 yields a liquid water velocity field equation

$$\mathbf{u}_l = -\frac{k_p^l}{\mu_l} \nabla p_g + \frac{k_p^l}{\mu_l} \frac{\partial p_c}{\partial s} \nabla s = -s \frac{k_p^0}{\mu_l} \nabla p_g - \mathcal{D}(s) \nabla s \quad [10]$$

where the diffusivity $\mathcal{D}(s)$ is defined as²⁰

$$\mathcal{D}(s) = -s \frac{k_p^0}{\mu_l} \frac{\partial p_c}{\partial s} \quad [11]$$

The functional variation of capillary pressure with saturation $p_c(s)$ is prescribed following Leverett²² who has shown that

$$p_c = \sigma \left(\frac{\varepsilon}{k_p^0} \right)^{1/2} f(s) \quad [12]$$

where σ is the interfacial liquid/gas tension, ε is the porosity, and $f(s)$ is the empirical function proposed by Udell²³

$$f(s) = 1.417(1-s) - 2.12(1-s)^2 + 1.263(1-s)^3 \quad [13]$$

Note that the above expression merely describes the overall shape of the capillary pressure function as a function of saturation, which is of cubic nature, whereas Eq. 12 provides the order of magnitude, which is predominantly determined by the permeability k_p^0 . This parameter varies over several orders of magnitude in the literature (e.g., Ref. 2 and 18).

An alternative expression for the liquid water velocity was suggested by Natarajan and Nguyen,¹⁷ who, however, neglected the convective part of the liquid water velocity

$$\mathbf{u}_l = -s \frac{k_p^0 \rho_l}{\mu_l} g \left(-\frac{\partial \psi}{\partial s} \right) \nabla s \quad [14]$$

where ρ_l is the liquid water density and g is gravity. The term $\partial \psi / \partial s$ is the functional that describes the dependence of permeability and capillary head on saturation, according to

$$\frac{\partial \psi}{\partial s} = -A \times D \{ e^{A(s-C)} + e^{-A(s-C)} \} \quad [15]$$

where A , C , and D are constants equal to 3.7, 0.494, and 0.0173 cm, respectively. Again a liquid water diffusivity can be defined

$$\mathcal{D}(s) = s \frac{k_p^0 \rho_l}{\mu_l} g \left(-\frac{\partial \psi}{\partial s} \right) \quad [16]$$

Figure 2 shows the liquid water diffusivities prescribed by Wang *et al.* based on Leverett's relation and using a dry electrode permeability of $k_p^0 = 10^{-10} \text{ cm}^2$. The corresponding liquid water diffusivities obtained by Natarajan and Nguyen¹⁷ are four orders of magnitude smaller, which means that extremely high saturation gradients would be necessary in order to induce the flux of liquid water. This explains why the results reported in Ref. 17 show liquid water saturations close to unity under the shoulders of the collector plate and near the catalyst layer. It should be noted that the function proposed by Leverett is based on experimental data in soil-like porous media,

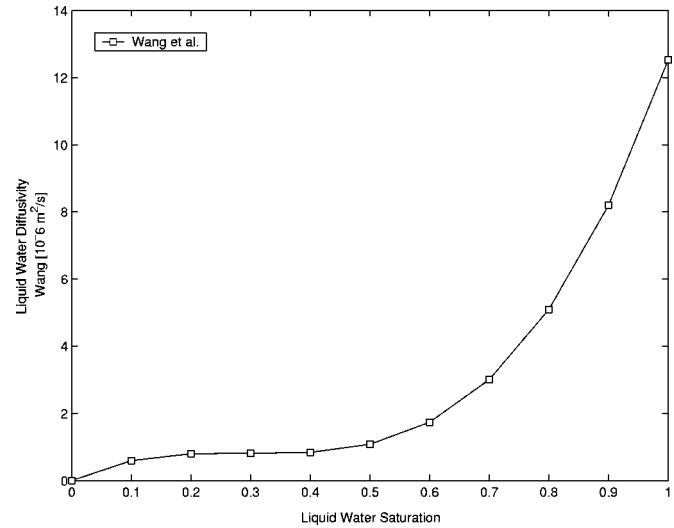


Figure 2. Variation of the liquid water diffusivity as a function of saturation using the Leverett's relation.

whereas Natarajan and Nguyen adjusted their data to fit their predicted polarization curve to measurements. It is nonetheless difficult to explain a four-order of magnitude differences between the liquid water diffusivity in soils and a porous gas diffusion layers, and clearly experimental data is required to resolve this issue. In the present study we use Leverett's function to determine the liquid water diffusivity.

The liquid phase consists of pure water, while the gas phase has multicomponents. The transport of each species in the gas phase is governed by a general convection-diffusion equation in conjunction which the Stefan-Maxwell equations to account for multispecies diffusion, as described in Ref. 14, 24, with the addition of a source term accounting for phase change

$$\nabla \cdot [r_g(\varepsilon_g \rho_g \mathbf{u}_g y_{gw} - \varepsilon_g D_{gi} \nabla y_{gw})] = \varepsilon_g (r_g S_{gw} + \dot{m}_{\text{phase}}) \quad [17]$$

where y_{gw} is the mass fraction of water vapor.

The energy equation reads as follows

$$\nabla \cdot [r_g(\varepsilon_g \rho_g \mathbf{u}_g H_g - \varepsilon_g \lambda_g \nabla T_g)] = -\varepsilon_g \dot{m}_{\text{phase}} \Delta H_{\text{evap}} \quad [18]$$

where ΔH_{evap} denotes the heat of evaporation or condensation in [J/kg] at 80°C. The gas phase and the liquid phase are assumed to be in thermodynamic equilibrium, *i.e.*, the liquid water and the gas phase are at the same temperature.

Implementation of phase change.—In order to account for the magnitude of phase change inside the GDL, expressions are required to relate the level of over- and undersaturation as well as the amount of liquid water present to the amount of water undergoing phase change. In the case of evaporation, such relations must be dependent on (i) the level of undersaturation of the gas phase in each control volume and on (ii) the surface area of the liquid water in the control volume. The surface area can be assumed proportional to the volume fraction of the liquid water in each cell. A plausible choice for the shape of the liquid water is droplets, especially since the catalyst area is Teflonated.

The evaporation rate of a droplet in a convective stream depends on the rate of undersaturation, the surface area of the liquid droplet, and a (diffusivity dependent) mass-transfer coefficient. The flux of water due to phase change can be represented by²⁵

$$\dot{N}_w = k_{xm} \pi D^2 \frac{x_{w0} - x_{w\infty}}{1 - x_{w0}} \quad [19]$$

where D is the diameter of the droplet, x_{w0} is the molar concentration of water at the gas/liquid interface, $x_{w\infty}$ is the bulk concentration of water vapor, k_{xm} is the transfer rate of water in $[\text{mol}/(\text{m}^2\text{s})]$ and \dot{N}_w is the flux of water from the liquid phase into the gas phase in $[\text{mol}/\text{s}]$. The bulk concentration $x_{w\infty}$ is known by solving the continuity equation of water vapor. To obtain the concentration at the surface, it is reasonable to assume thermodynamic equilibrium between the liquid phase and the gas phase at the interface, *i.e.*, the relative humidity of the gas in the immediate vicinity of the liquid is 100%. Under that condition, the surface concentration can be calculated based on the saturation pressure and is only a function of temperature.

The heat-transfer coefficient for convection around a sphere is well established, and by invoking the analogy between convective heat and mass transfer, the following mass-transfer coefficient k_{xm} is obtained²⁵

$$k_{xm} = \frac{c_g D_{wg}}{D} \left[2.0 + 0.60 \left(\frac{D v_\infty \rho_g}{\mu_g} \right)^{1/2} \left(\frac{\mu_g}{\rho_g D_{wg}} \right)^{1/3} \right] \quad [20]$$

where c_g is the concentration of air in $[\text{mol}/\text{m}^3]$, D_{wg} is the diffusion coefficient of water-vapor in air in $[\text{m}^2/\text{s}]$, v_∞ is the free-stream velocity in $[\text{m}/\text{s}]$, and ρ_g is the air density in $[\text{kg}/\text{m}^3]$. All these properties can be readily calculated. It should be noted that both the heat-mass transfer analogy and the above correlation were derived for boundary-layer-type of flow. Fundamental work is required to establish alternative relations for droplet evaporation in a porous medium. In any case since only an order of magnitude estimate of the evaporation rate is required for the numerical procedure to attain equilibrium, this approach is adequate in the context of this study.

It is further assumed that all droplets have a specified diameter D , and the number of droplets in each control volume is found by dividing the total volume of the liquid phase in each control volume by the volume of one droplet

$$N_{D,CV} = \frac{r_1 V_{CV}}{\frac{1}{6} \pi D^3} \quad [21]$$

The above expression can be used to obtain an order of magnitude for the rate of evaporation of the liquid water in each control volume. Because the choice of nominal droplet size is subject to a large uncertainty, along with the assumption that the droplets either exist or not (they do not shrink due to evaporation) the overall expression is scaled by a factor ψ , so that the overall molar flux for a given control volume is given by

$$\dot{N}_w = \psi N_{D,CV} k_{xm} \pi D^2 \frac{x_{w0} - x_{w\infty}}{1 - x_{w0}} \quad [22]$$

The sensitivity of the solution to ψ was assessed by varying its value by orders of magnitude. For evaporation-driven cases, the relative humidity of the gas phase was found to remain 100% for values of ψ several orders of magnitude smaller than 1.0, confirming that the rate of evaporation is indeed fast enough to justify the commonly used assumption of a fully humidified gas phase.

In the case when the calculated relative humidity in a control volume exceeds 100% condensation occurs. The case of condensation is more complex, because it can occur on every solid surface area, but the rate of condensation can be different when it takes place on a wetted surface. In addition, the overall surface area in each control volume available for condensation shrinks with an increasing amount of liquid water present. In the current implementation, we assume the rate of condensation depends only on the level of oversaturation of the gas phase multiplied by a constant. This is believed to be a good approximation for low saturation values. In case the saturation is high, the shrinkage of the available condensa-

Table I. Geometrical, operational, and transport parameters at base case conditions.

Parameter	Symbol	Value	Unit
Channel length	l	0.03	m
Electrode thickness	t_e	0.20×10^{-3}	m
Inlet fuel and air temperature	T	60	°C
Air side pressure	p_c	1	atm
Fuel side pressure	p_a	1	atm
Relative humidity of inlet gases	ξ	100	%
Electrode porosity	ε	0.5	-
Dry hydraulic permeability	k_p^0	10^{-14}	m^2
Condensation constant	C	10^{-5}	
Surface tension	σ	6.25	N/cm
Enthalpy of evaporation	ΔH_{evap}	2.36×10^6	J/kg
Liquid water diffusivity in channels	D_l	10^{-5}	m^2/s
Water-vapor diffusivity	D_{wg}	2.92×10^{-5}	m^2/s
Binary diffusivity ($T_{\text{ref}} = 307.1$ K)	$D_{\text{H}_2-\text{H}_2\text{O}}$	0.915	cm^2/s
Binary diffusivity ($T_{\text{ref}} = 298.0$ K)	$D_{\text{H}_2-\text{CO}_2}$	0.646	cm^2/s
Binary diffusivity ($T_{\text{ref}} = 307.5$ K)	$D_{\text{H}_2\text{O}-\text{CO}_2}$	0.202	cm^2/s
Binary diffusivity ($T_{\text{ref}} = 308.1$ K)	$D_{\text{O}_2-\text{H}_2\text{O}}$	0.282	cm^2/s
Binary diffusivity ($T_{\text{ref}} = 293.2$ K)	$D_{\text{O}_2-\text{N}_2}$	0.220	cm^2/s
Binary diffusivity ($T_{\text{ref}} = 307.5$ K)	$D_{\text{H}_2\text{O}-\text{N}_2}$	0.256	cm^2/s

tion surface area with an increasing saturation has to be accounted for. We see in the Results section, however, that the predicted local saturation values do not exceed 10%. For operating conditions or designs resulting in high levels of liquid saturation, a more general approach would need to be implemented. Thus

$$\dot{m}_{\text{cond}} = -\psi C \frac{x_{w0} - x_{w\infty}}{1 - x_{w0}} \quad [23]$$

Catalyst layers.—The catalyst layers are treated as thin interfaces, where the oxygen and hydrogen are depleted and liquid water and heat are produced. The depletion and production rates depend on the local current density i , which is described by the Tafel equation. In common with most other multidimensional modeling studies, a simplification is introduced by assuming a constant local activation overpotential η . The local current density at the cathode side becomes thus a function of the local oxygen distribution only. This approach allows the use of the average current density as an input variable when performing systematic simulations for various operating parameters such as the stoichiometric flow ratio. For details, please refer to Ref. 14 and 24.

Cooling water channel.—In the water channel, the Navier-Stokes equations and the energy equation for an incompressible fluid are solved, *i.e.*, the continuity equation

$$\nabla \cdot (\rho_l \mathbf{u}_l) = 0 \quad [24]$$

the momentum equation

$$\nabla \cdot (\rho_l \mathbf{u}_l \times \mathbf{u}_l - \mu_l \nabla \mathbf{u}_l) = -\nabla \left(p + \frac{2}{3} \mu_l \nabla \mathbf{u}_l \right) + \nabla \cdot [\mu_l (\nabla \mathbf{u}_l)^T] \quad [25]$$

and the energy equation

$$\nabla \cdot (\rho_l \mathbf{u}_l H_l - \lambda_l \nabla T_l) = 0 \quad [26]$$

where the total enthalpy \mathbf{H} is calculated using the static (thermodynamic) enthalpy h

$$H_l = h_l + \frac{1}{2} \mathbf{u}_l^2 \quad [27]$$

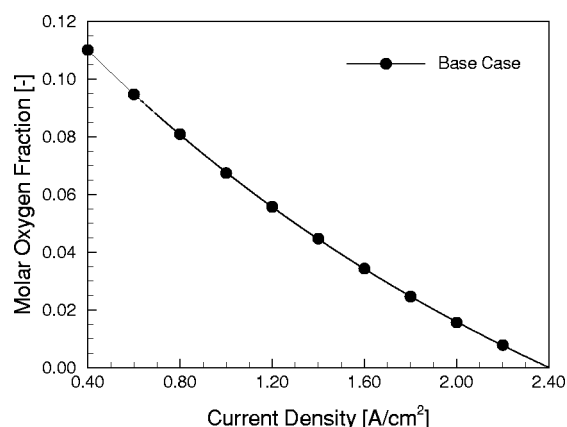


Figure 3. Average molar oxygen concentration at the catalyst layer as function of the current density.

The fluid in the cooling channels is assumed to be pure liquid water, hence, no additional species equation is required.

Graphite plates.—The collector plates consist of graphite and serve to transfer electrons towards the gas-diffusion layers and to the reaction sites (current collectors). Currently, only heat conduction is considered in the solid plates

$$\nabla \cdot (\lambda_{gr} \nabla T) = 0 \quad [28]$$

Boundary conditions.—Symmetry boundary conditions are applied in the z direction and the y directions, thereby reducing the size of the computational domain and computational costs. In the x direction, zero flux conditions are applied at all interfaces except for the flow channels. At the inlets of the gas-flow channels, the incoming velocity is calculated as a function of the desired current density and stoichiometric flow ratio, as described in Ref. 14. At the outlets, the pressure is prescribed for the momentum equation and a zero-gradient conditions is imposed for all scalar equations. For the water cooling channel, the inlet velocity and the temperature are specified.

Modeling parameters.—With the exception of the parameters listed in Table I, the physicochemical and geometric parameters are identical to those used in the single-phase simulations of Berning *et al.*¹⁴ The reference binary diffusivities for the Stefan-Maxwell equation are listed and were scaled for temperature and pressure using

$$D_{ij} = D_{ij}(T_0, p_0) \frac{p}{p_0} \left(\frac{T}{T_0} \right)^{1.5} \quad [29]$$

In order to reduce the computational requirements, which are much higher for the two-phase flow model, the channel length has been shortened from 5 to 3 cm. The thickness of the gas diffusion layer is 0.2 mm with a porosity of 0.5. Operation is assumed at atmospheric pressure and at a nominal temperature of 60°C, and the incoming gases are fully humidified. It was mentioned before that in the multiphase case the permeability of the dry electrode becomes one of the central parameters. A value of 10^{-10} cm^2 is used, which is consistent with the value used by Natarajan and Nguyen.¹⁷ As the values for the permeability cited in the literature range over orders of magnitude, this will be an important parameter to investigate in the future.

The last parameters listed in Table I are specific to the multiphase flow and phase change. The condensation constant has been adjusted so that the relative humidity inside the gas diffusion layers remains below 100.1%, assuming fast condensation, which is not limited by mass transport to and from the condensation surfaces. A standard value was used for the enthalpy of evaporation (*e.g.*, Ref. 26).

The droplet size and the scaling parameter for evaporation were adjusted so that the relative humidity inside the gas diffusion layer remained above 99.9% in the presence of liquid water, again assuming a fast rate of phase change.

Numerical procedure.—The model presented here was implemented into a commercial computational fluid dynamics code (CFX 4.3 from AEA Technology). In order to accommodate the various transport mechanisms, an extensive suite of user subroutines had to be implemented along with customized iteration procedures. A single data point required approximately 10,000 iterations, and most of the simulations were performed on a single node of an IBM SP2 computer. Due to the complexity of this model with a large spatial variation in competing transport and phase-change mechanisms, convergence was assumed when the overall mass imbalance was below 0.1%.

Results and Discussion

Prior to proceeding with a detailed analysis of the results, it is useful to discuss some of the phase-change mechanisms. The central parameter for determining the direction of phase change is the relative humidity of the gas phase

$$\phi = \frac{p_{\text{H}_2\text{O}}}{p_{\text{sat}}(T)} \quad [30]$$

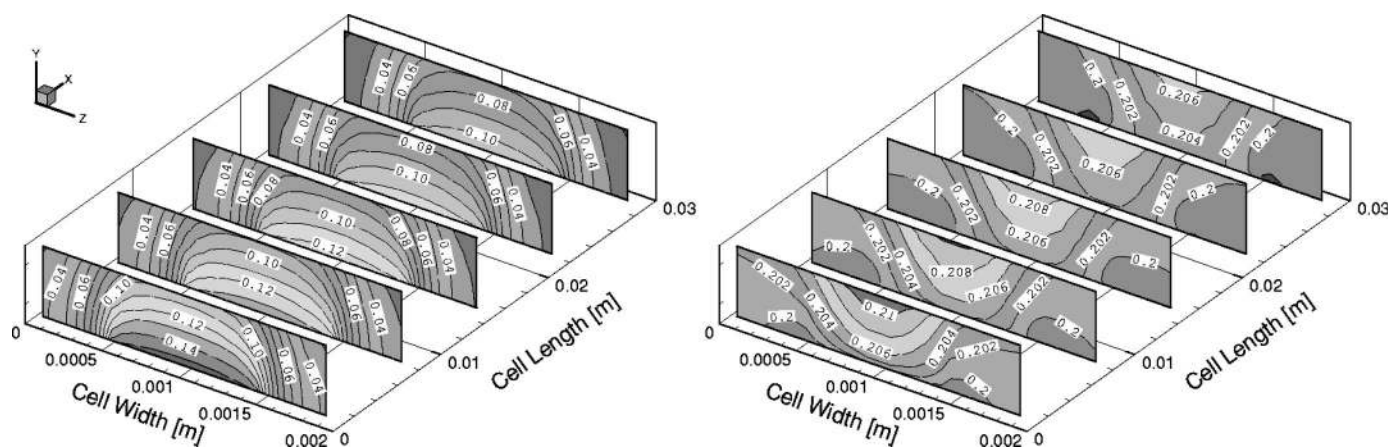


Figure 4. Molar oxygen (left) and water vapor (right) fraction inside the cathodic gas-diffusion layer at a current density of 1.2 A/cm². The cathode-catalyst layer correspond to the upper side and the cathode-channel interface to the lower.

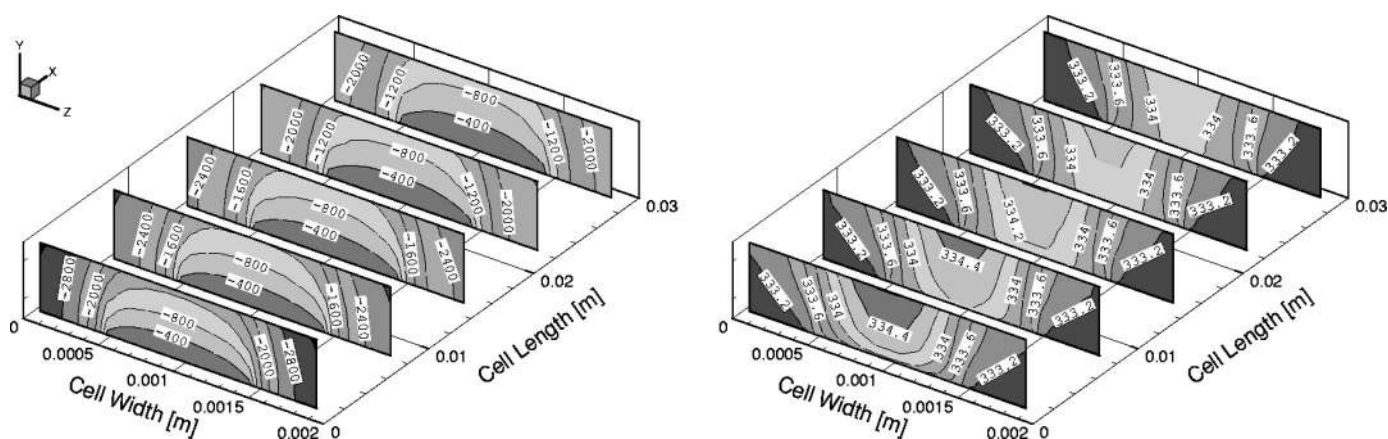


Figure 5. Pressure drop [Pa] and temperature distribution [K] inside the cathodic gas-diffusion layer at a current density of 1.2 A/cm^2 . (Cathode-catalyst layer corresponds to the upper side and the cathode-channel interface to the lower.)

i.e., the ratio of partial pressure of the water vapor in the gas phase to the saturation pressure p_{sat} , which is a function of temperature only. According to Dalton's law the partial pressure of a species is equal to its molar fraction x multiplied with the total pressure of the gas phase p_g , *i.e.*,

$$\phi = x_{\text{H}_2\text{O}} \frac{p_g}{p_{\text{sat}}(T)} \quad [31]$$

When the relative humidity is below 1.0 (or 100%) in the presence of liquid water, this give rise to evaporation. Condensation, on the other hand, occurs when the relative humidity exceeds 100% in the presence of condensation surfaces, which are in abundance inside the gas-diffusion layer. The gas-diffusion layer of a PEM fuel cell is particularly interesting for phase-change considerations, because all three parameters on the right side of Eq. 31 vary, resulting in competing directions of phase change as follows.

1. The molar water fraction $x_{\text{H}_2\text{O}}$ increases inside the GDL, simply as a result of reactant consumption. Provided the relative humidity of the incoming air is at 100%, this process alone would lead to condensation.

2. The thermodynamic pressure p_g of the gas-phase changes inside the GDL. This is a very interesting effect and, depending on the incoming gas condition, it can lead to either evaporation or condensation. In the first place, there is a pressure drop inside the GDL due again to reactants consumption. This pressure drop depends strongly

on the permeability of the gas-diffusion layer, *i.e.*, for the same amount of consumed reactants, the pressure drop will be higher for a lower permeability. The bulk velocity of the gas phase is directed into the GDL, and is governed by Darcy's law. Thus, the pressure drop inside the GDL depends strongly on the permeability. The partial pressure of the water vapor decreases with the gas-phase pressure p_g . Hence, this effect alone would lead to undersaturation, causing evaporation. A special case arises when the incoming air is relatively dry, in which case most of the product water will evaporate. The cathodic half-cell reaction produces two water molecules for each oxygen molecule consumed. This means that for high evaporation rates, every oxygen molecule inside the gas phase will be replaced by two water vapor molecules, thereby causing an increase in the gas-phase pressure. As a result, the bulk flow of the gas phase would then be directed from the catalyst layer towards the channel, as has been observed by Wang *et al.*¹⁸ This means that the oxygen would have to diffuse towards the catalyst interface against the bulk flow of the gas phase, which will possibly cause a decrease in the limiting-current density.

3. The saturation pressure $p_{\text{sat}}(T)$ increases with an increase in temperature caused by the heat production term due to the electrochemical reaction. The order of magnitude of the temperature increase depends primarily on the thermal conductivity of the gas-diffusion layer. It was found with an earlier version of this model that the temperature can rise by a few degrees Kelvin,¹⁴ and this effect alone would lead to evaporation of liquid water.

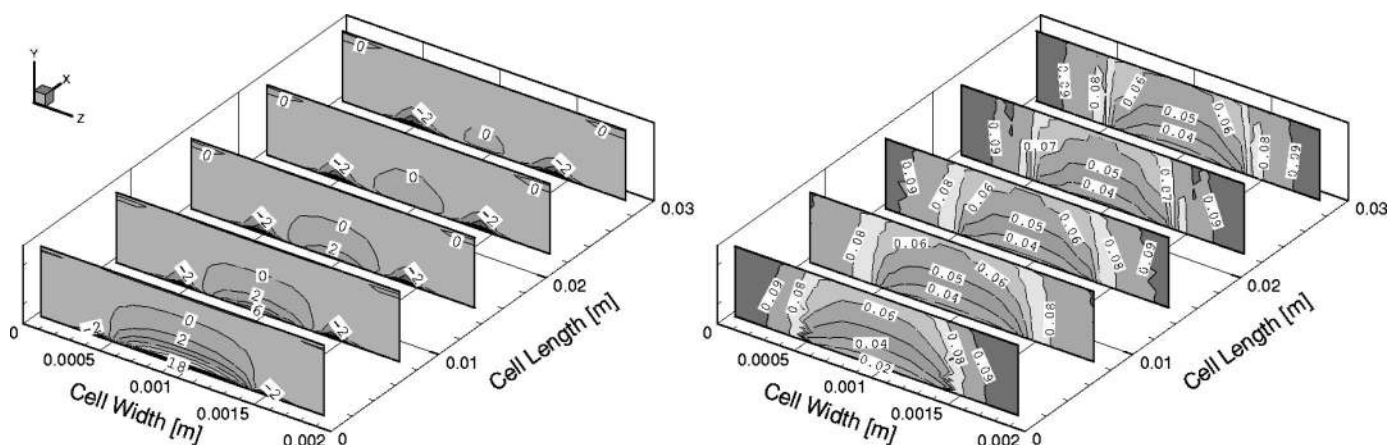


Figure 6. Rate of phase change (left) in $[\text{kg}/(\text{m}^3 \text{ s})]$ and liquid water saturation (right) inside the cathodic gas-diffusion layer at a current density of 1.2 A/m^2 . (Cathode-catalyst layer correspond to the upper side and the cathode-channel interface to the lower.)

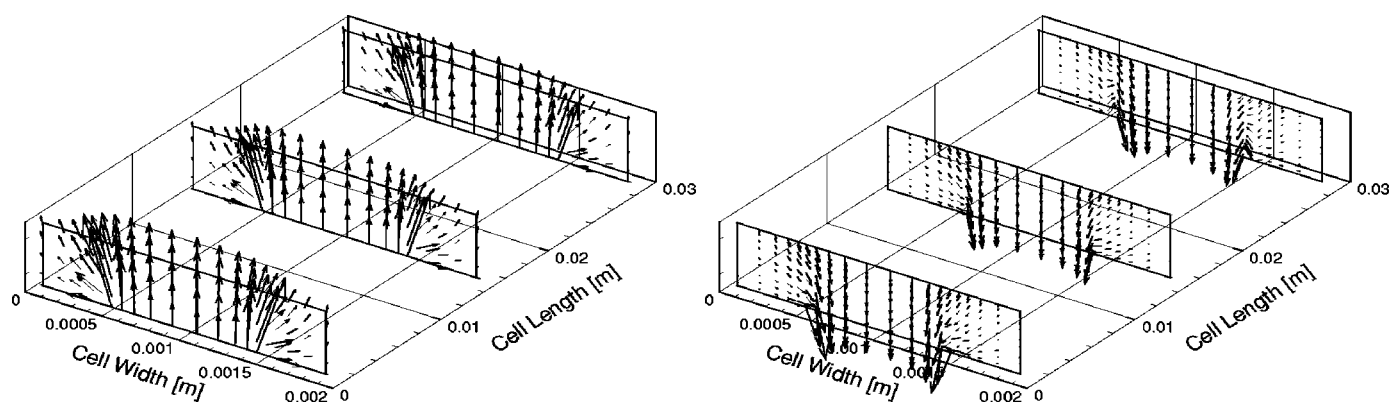


Figure 7. Gas-phase velocity vectors (left) and liquid water velocity vectors (right) inside the cathodic gas-diffusion layer at a current density of 1.2 A/cm^2 . The vector scaling is $5[(\text{cm/s})/\text{cm}]$ for the gas phase and $200[(\text{cm}/(\text{cm/s}))]$ for the liquid phase. (Cathode-catalyst layer correspond to the upper side and the cathode-channel interface to the lower.)

The net phase change is a result of the balance between these competing, coupled, and spatially varying mechanisms. It should be noted that the first two effects are also of importance inside the gas flow channels; the oxygen depletion from inlet to outlet results in oversaturation and condensation at the walls and channel/GDL interface, whereas the overall pressure drop along the channel would alone cause evaporation. For the straight channel section considered here, the total pressure drop is relatively small and hence the oxygen depletion effect dominates, causing condensation. The dominant mechanisms highlighted in this discussion are relevant to cases where the incoming air is at a high humidification level, as is the case in practical fuel cell operation.

Cathode side transport.—Investigations of phase-change behavior are usually focused on the cathode side, since this is where water is produced. Also, mass-transport limitations are almost always associated with the cathode. An estimate of the limiting current density for the case considered in this paper can be obtained by examining the average molar oxygen fraction at the catalyst layer as function of current density, shown in Fig. 3. The maximum current density predicted is about 2.4 A/cm^2 . This relatively high current is due to the high oxygen molar fraction brought about by the low water vapor molar fraction dictated by the relatively low operating temperature of 60°C , as well as to the high stoichiometric flow ratio of 3.0 and a relatively high gas diffusion layer of 0.5. A detailed numerical parametric study²⁷ shows that these parameters greatly influence the limiting-current density, and a recent experimental

parametric study reports comparable limiting current densities for similar operating and humidification temperatures.²⁸

The discussion and detailed analysis focuses on simulations corresponding to a current density of 1.2 A/cm^2 . Figure 4 shows the oxidant and water vapor distributions inside the cathode. Note that as pointed out earlier, the simulations take advantage of the symmetry of the system and only include half of channel and half of the land area. For clarity, the solutions are mirrored and a full channel and the adjacent land areas are displayed in the results. The oxygen concentration at the catalyst layer is qualitatively similar to that predicted in single-phase simulations. It is highest under the channel, and exhibits a three-dimensional behavior with a fairly significant drop under the land areas, and a more gradual depletion towards the outlet. The molar water vapor fraction, however, remains almost constant throughout the gas-diffusion layer. In the absence of phase change, this would not be the case, as the nitrogen and water vapor fraction would increase as the oxygen fraction decreases.

Figure 5 shows the pressure distribution and temperature distribution inside the cathodic gas-diffusion layer at the same current density. Clearly, the pressure drop inside the gas-diffusion layer varies strongly with the hydraulic permeability of the carbon fiber paper. The permeability is set at 10^{-10} cm^2 in this study, but as pointed out earlier, values ranging over several orders of magnitude are found in the literature. The magnitude of the pressure drop significantly impacts the magnitude of the evaporation term according to Eq. 31; this and the effect of varying permeability was beyond the

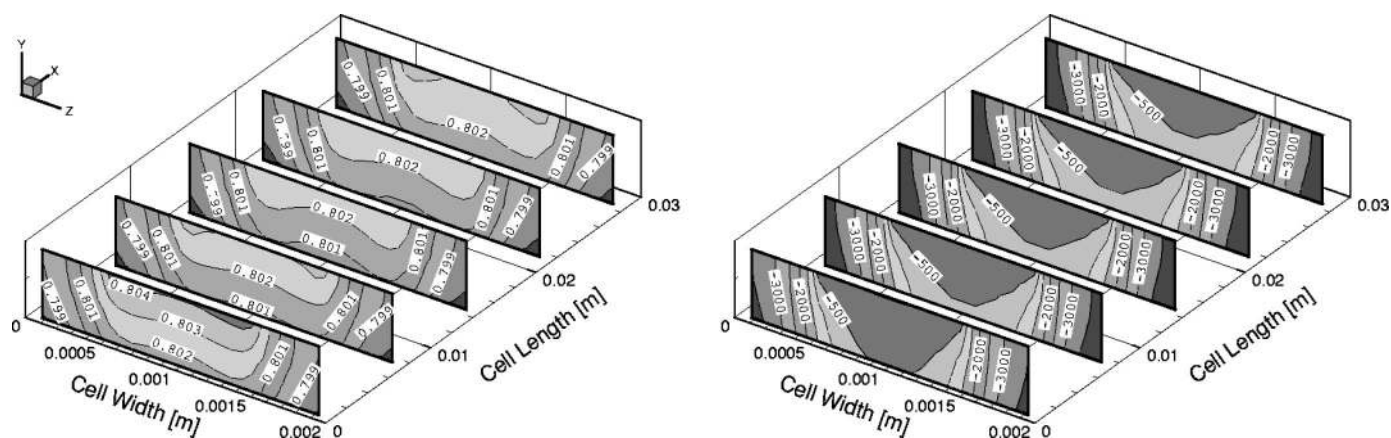


Figure 8. Molar hydrogen fraction (left) and pressure drop [Pa] inside the anodic gas-diffusion layer at a current density of 1.2 A/cm^2 . (Cathode-channel interface correspond to the upper side and the cathode-catalyst interface to the lower.)

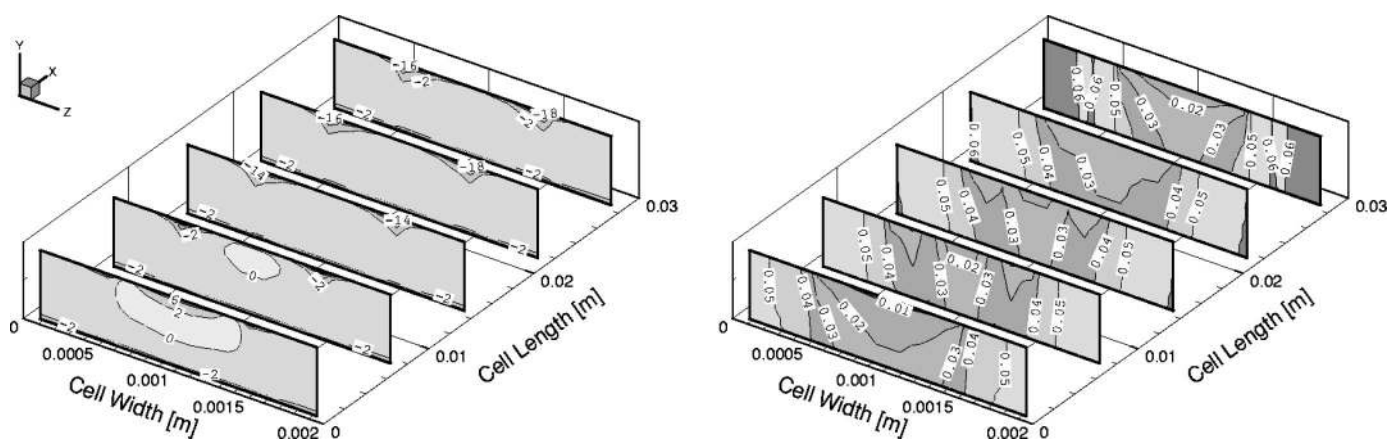


Figure 9. Rate of phase change (left) in $[\text{kg}/(\text{sm}^3)]$ and liquid water saturation (right) inside the anodic gas-diffusion layer at a current density of $1.2 \text{ A}/\text{cm}^2$. (Cathode-channel interface correspond to the upper side and the cathode-catalyst interface to the lower.)

scope of the present study. It should be noted that in the case analyzed here a pressure drop occurs partly because of the fully humidified incoming gas at the cathode side. With a dry inlet cathode gas stream, most of the product water will evaporate, but, since for every reacting oxygen molecule two water molecules are produced in the gas phase, the gas phase pressure will therefore increase. This can in fact be observed in the low inlet humidity simulations of Wang *et al.*¹⁸ The effect of phase change on the temperature distribution is small overall in this particular case, mostly because of the fully humidified inlet gases that result in a low amount of net phase change. The small temperature increase at the catalyst layer is primarily due to the heat production term implemented here.¹⁴

The rate of phase change and the resulting liquid water saturation are shown in Fig. 6. Slight condensation occurs almost throughout the GDL (values being between -2 and 0). The condensation caused by the oxygen depletion effect appears to be the dominant effect in this particular case. A strong evaporation term exists at the interface between the GDL and the channel, particularly at the inlet. In this area the oxygen depletion effect is not yet significant and is outweighed by the combined effect of pressure drop and temperature increase. The resulting liquid water saturation in the cathodic GDL is below 10% throughout the entire GDL, with maximum saturations found under the land area. The high spatial variation of the saturation demonstrates again the three-dimensional nature of transport processes in PEMFCs. The range of liquid water saturations predicted here is similar to that reported by Wang *et al.*¹⁸ and You

and Liu.¹⁹ Natarajan and Nguyen¹⁷ reported liquid water saturation levels close to 100% near the catalyst and under the shoulders, in spite of the completely dry incoming gas stream. As discussed earlier this is a consequence of the extremely low liquid water diffusivity chosen in that study. Clearly, liquid water saturation depends strongly on the specified capillary pressure function (Eq. 12 and 13) and again, the permeability of the gas-diffusion layer becomes the central parameter.

The velocity field inside the cathodic gas-diffusion layer is shown in Fig. 7. The pressure gradient induces bulk gas flow from the channels into the GDL. This is in contrast with the low humidity inlet stream case (high evaporation) results of Wang *et al.* where the flux is directed from the GDL to the channel. The maximum velocity in the y direction is around $7.8 \times 10^{-3} \text{ m/s}$, and is thus of the same order of magnitude as that reported in Ref. 18. The liquid water flux is directed from the GDL into the channel, *i.e.*, in the opposite direction of the gas-phase velocity. The highest value of the liquid-phase velocity is around $2.5 \times 10^{-4} \text{ m/s}$, occurring under the elbow of the collector plate land. Inside the GDL the liquid water velocity is in the range of 10^{-5} m/s .

Anode side transport.—One of the unique features of the multiphase model presented here is that the anode side is included as well. The underlying mechanisms of phase change are the same for cathode and anode sides, but their magnitudes differ and in addition the phase-change process takes place in a binary rather than a ternary

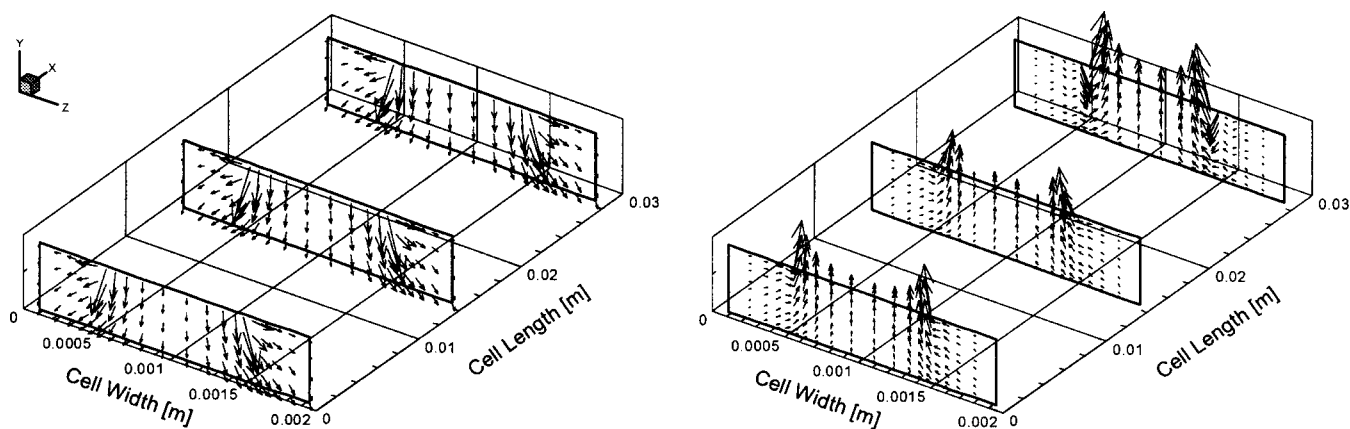


Figure 10. Gas-phase velocity vectors (left) and liquid water velocity vectors (right) inside the anodic gas-diffusion layer at a current density of $1.2 \text{ A}/\text{cm}^2$. The vector scaling is $5[(\text{cm/s})/\text{cm}]$ for the gas phase and $200[(\text{cm/s})/\text{cm}]$ for the liquid phase. (Cathode-channel interface correspond to the upper side and the cathode-catalyst interface to the lower.)

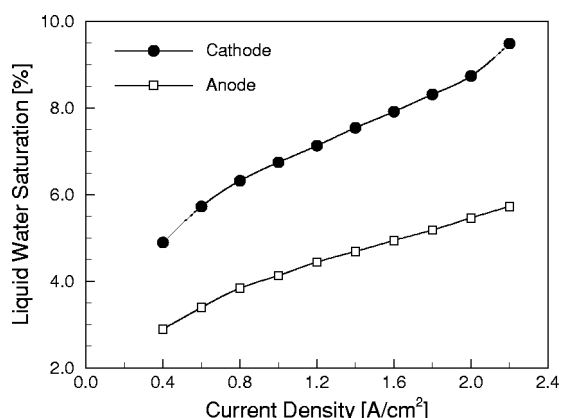


Figure 11. Average liquid water saturation inside the gas-diffusion layers as a function of current density.

mixture. Figure 8 shows the gas-phase pressure and the hydrogen distribution inside the anodic gas-diffusion layer. The molar hydrogen fraction is almost constant inside the GDL. This may seem surprising initially, but is explained by the fact that consumption of hydrogen leads to a direct increase of the molar water vapor fraction since the anode gas stream is a binary mixture, and hence a high level of oversaturation (see Eq. 31) results in a strong condensation potential inside the gas-diffusion layer. This in turn affects the gas-phase pressure. The pressure drop inside the anodic gas diffusion layer is higher than the one at the cathode, because of the high condensation terms here. The virtually constant hydrogen molar fraction is a particularly interesting feature when considering that transport of the reactants towards the catalyst is predominantly via diffusion.

Figure 9 shows the rate of evaporation and the liquid water saturation in the anodic gas-diffusion layer. As pointed out above, condensation occurs throughout the GDL due to hydrogen depletion. Liquid water is thus produced inside the anodic GDL, which should help counteract the tendency for membrane dehumidification observed on the anode side in previous studies.³ Transport or driving out of (condensed) liquid water in the GDL towards the channel requires the build up of a sufficient capillary pressure. The resulting liquid water saturation is presented in the right side of Fig. 9. The overall saturation for the conditions considered is lower than at the cathode side. Since the predicted saturation levels depend primarily on the capillary pressure function, it is clear that the permeability of the carbon fiber paper plays a determining role.

The velocity of both gas and liquid phases at the anode are shown in Fig. 10. The gas-phase velocity direction is always directed from the channel to the GDL, as there is no product water that can evaporate. The maximum velocity at the anode side is relatively high, around 1.4×10^{-2} m/s. The liquid water velocity field in the anodes exhibits a similar pattern to that in the cathodes with a maximum velocity of about 1.1×10^{-4} m/s.

Bulk mass-transport balance.—Figure 11 shows the liquid water saturation, averaged over the entire cell, as a function of current density. The average liquid water saturation inside the gas diffusion layers increases in a nonlinear monotonic fashion for both anode and cathode sides. The volume fraction of liquid water remains below 10% at the cathode side and 6% at the anode side for all current densities. This suggests that it should be possible to keep the membrane fully humidified without an external humidification scheme, particularly on the anode side, and it would be interesting to investigate and verify this experimentally. A liquid water saturation value of 10% is far below the pore-plugging regime, and it will be interesting to explore in the future under what conditions this level of saturation rises and to what extent.

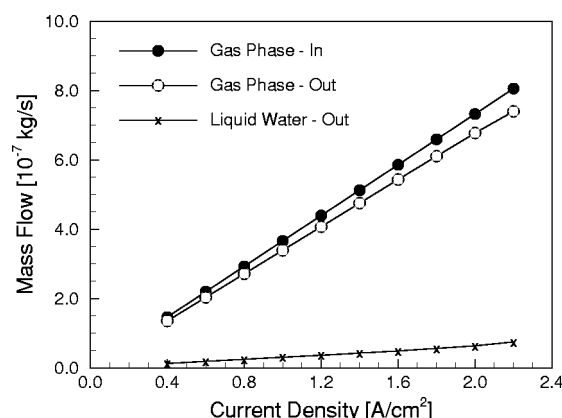


Figure 12. Mass flow balance for the cathode side at 60°C.

The overall mass flow balances for cathode and anode side are shown in Fig. 12 and 13, respectively. In both cases, the amount of liquid water leaving the cell increases almost linearly with the current density, and the mass flow rate is roughly an order of magnitude smaller than the mass flow of the gas phase. The small difference between outlet and inlet mass flow rates at the cathode is another indication of the relatively small evaporation rate of product water. This is also demonstrated by examining the net phase change plotted in Fig. 14 for various current densities. The net phase change is negative on both cathode and anode sides, implying that on average and in addition to product water, incoming water vapor condenses when transiting through the cell. The zero line corresponds to a situation where all product water would leave the cell in the liquid phase.

Conclusions

A three-dimensional computational model of a PEM fuel cell has been developed. This model includes multiphase multicomponent transport and heat transfer for both cathode and anode. Simulations performed with this model for operation with fully humidified reactant streams show that the liquid water volume fraction (saturation) increases nonlinearly with increasing current density. Phase change is driven by the balance of three separate processes, temperature change, reactant gas depletion, and pressure drop inside the GDL which combined contribute to evaporation or condensation in a non-intuitive manner. The predicted saturation levels depend heavily on the permeability of the diffusion material. A systematic parametric study of the effect of permeability was beyond the scope of the present study, but results indicate that for large values of the GDL permeability, liquid water saturation in excess of 20% can be at-

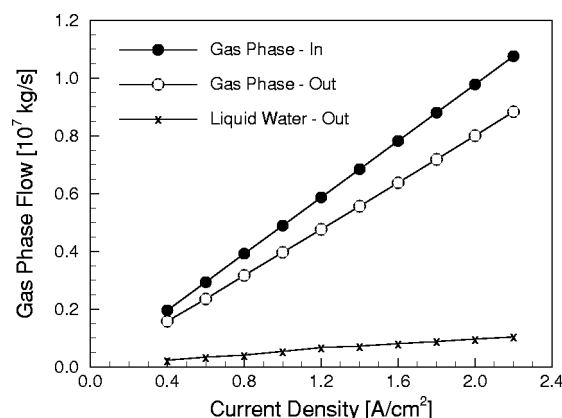


Figure 13. Mass flow balance at the anode side at an operating temperature of 60°C.

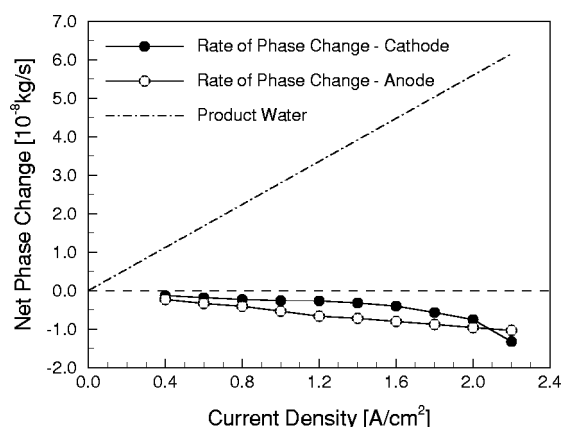


Figure 14. Rate of phase change inside the gas diffusion layers. Negative values indicate overall condensation. Average rate of production of water through the electrochemical reaction is shown for reference.

tained at the anode side. These saturation levels decrease with permeability because all of the liquid water at the anode is produced by condensation at the channel/GDL interface. At the cathode side, the opposite is true, the liquid water saturation increases with decreasing permeability, because most of the water is produced via the electrochemical reaction and can become trapped inside the GDL. The level of saturation decreases with increasing permeability.

The simulations presented in this paper clearly illustrate the three-dimensional nature of the transport mechanisms, fluxes, and resulting distributions of reactants, temperature, pressure, and water. The model provides several improvements and allows simulations under representative operating conditions, including high inlet humidity, but the added complexity comes with a significantly higher computational overhead. In addition to investigating the effect of permeability and wetting (Teflonation) characteristics of the gas diffusion electrode material, future work will focus on incorporating

membrane transport and fully coupling the anode and cathode transport, as well as on implementing more efficient numerical strategies, including parallel computing to allow practical use of the model for systematic parametric studies. It is clear that further progress on these fronts will require not only validation data under well-documented operating conditions but also experimental data for many of the transport parameters of the gas-diffusion electrode.

The University of Victoria assisted in meeting the publication costs of this article.

References

1. D. M. Bernardi and M. W. Verbrugge, *AIChE J.*, **37**, 1151 (1991).
2. D. M. Bernardi and M. W. Verbrugge, *J. Electrochem. Soc.*, **139**, 2477 (1992).
3. T. E. Springer, T. A. Zawodzinski, and S. Gottesfeld, *J. Electrochem. Soc.*, **138**, 2334 (1991).
4. T. F. Fuller and J. Newman, *J. Electrochem. Soc.*, **140**, 1218 (1993).
5. T. V. Nguyen and R. E. White, *J. Electrochem. Soc.*, **140**, 2178 (1993).
6. J. S. Yi and T. V. Nguyen, *J. Electrochem. Soc.*, **145**, 1149 (1998).
7. J. S. Yi and T. V. Nguyen, *J. Electrochem. Soc.*, **146**, 38 (1999).
8. V. Gurau, H. Liu, and S. Kakac, *AIChE J.*, **44**, 2410 (1998).
9. S. Um, C. Y. Wang, and K. S. Chen, *J. Electrochem. Soc.*, **147**, 4485 (2000).
10. T. Zhou and H. Liu, *Int. J. Trans. Phenom.*, **3**, 177 (2001).
11. N. Djilali, D. M. Lu, and T. Berning, in *Proceedings of 1998 Fuel Cell Seminar*, pp. 562-565, Palm Springs, CA (1998).
12. N. Djilali, D. M. Lu, and T. Berning, in *Proceedings of 9th Canadian Hydrogen Conference*, pp. 589-601, Vancouver, BC (1999).
13. S. Dutta, S. Shimpalee, and J. W. Van Zee, *J. Appl. Electrochem.*, **30**, 135 (2000).
14. T. Berning, D. Lu, and N. Djilali, *J. Power Sources*, **106**, 284 (2002).
15. J. J. Baschuk and X. Li, *J. Power Sources*, **86**, 181 (2000).
16. S. Shimpalee and S. Dutta, *Int. J. Heat Mass Transf.*, **44**, 2029 (2001).
17. D. Natarajan and T. V. Nguyen, *J. Electrochem. Soc.*, **148**, A1324 (2001).
18. Z. H. Wang, C. Y. Wang, and K. S. Chen, *J. Power Sources*, **94**, 40 (2001).
19. L. You and H. Liu, *Int. J. Heat Mass Transf.*, **45**, 2277 (2002).
20. C. Y. Wang and P. Cheng, *Adv. Heat Transfer*, **30**, 93 (1997).
21. W. He, J. S. Yi, and T. V. Nguyen, *AIChE J.*, **46**, 2053 (2000).
22. M. C. Leverett, *Trans. Am. Inst. Min., Metall. Pet. Eng.*, **142**, 152 (1941).
23. K. S. Udell, *Int. J. Heat Mass Transf.*, **28**, 485 (1985).
24. T. Berning, Ph.D. Thesis, University of Victoria, Vancouver, BC (2002).
25. R. B. Bird, W. Steward, and E. N. Lightfoot, *Transport Phenomena*, Wiley, New York (1960).
26. M. J. Moran and H. N. Shapiro, *Fundamentals of Engineering Thermodynamics*, Wiley, New York (1995).
27. T. Berning and N. Djilali, *J. Power Sources*, Accepted.
28. L. Wang, A. Hussar, T. Zhou, and H. Liu, *Int. J. Hydrogen Energy*, **28**, 1263 (2003).